Applied Catalysis B: Environmental 111–112 (2012) 185–199

Contents lists available at SciVerse ScienceDirect

Applied Catalysis B: Environmental

journal homepage: www.elsevier.com/locate/apcatb

Preparation, characterization and single-cell performance of a new class of Pd-carbon nitride electrocatalysts for oxygen reduction reaction in PEMFCs

Vito Di Noto[a,*,1], Enrico Negro[a], Stefano Polizzi[b], Pietro Riello[b], Plamen Atanassov[c]

[a] Dipartimento di Scienze Chimiche, Università di Padova, Via Marzolo 1, I-35131 Padova (PD), Italy
[b] Dipartimento di Chimica Fisica, Università di Venezia, Via Torino 155/b, I-30172 Mestre (VE), Italy
[c] Chemical & Nuclear Engineering Department and Center for Emerging Energy Technology, University of New Mexico, Albuquerque, NM 87131, USA

ARTICLE INFO

Article history:
Received 16 May 2011
Received in revised form
18 September 2011
Accepted 25 September 2011
Available online 29 September 2011

Keywords:
PEM fuel cells
Carbon nitride electrocatalysts
XPS
CV-TF-RDE method
MEA preparation

ABSTRACT

This report describes the preparation of two Pd-based carbon nitride electrocatalysts for the oxygen reduction reaction (ORR) for application in polymer electrolyte membrane fuel cells (PEMFCs). The electrocatalysts consist of multi-metallic active sites supported on a graphite-like carbon nitride (CN) matrix with a N content exceeding 13 wt%. The electrochemical performance is investigated by cyclic voltammetry with the thin-film rotating disk electrode method (CV-TF-RDE) and evaluated in a single membrane electrode assembly (MEA) PEMFC. The correlation of the structural information to functional properties allows to propose a reaction mechanism and to identify the most desirable features to achieve in a CN electrocatalyst in order to obtain desired electrochemical performance in catalysis of ORR. It is established also that the CN support improves the tolerance towards the catalyst corrosion under oxidizing conditions and thus improves the catalyst durability. The stoichiometry and the morphology of Pd-based CN electrocatalysts play a crucial role in the modulation of the tolerance towards common ORR poisons such as chlorine anions and methanol. Finally, the performance of the Pd-based CN electrocatalysts in a single MEA PEMFC proved promising.

1. Introduction

Polymer electrolyte membrane fuel cells (PEMFCs) are a class of flow-through devices where the chemical energy of the reagents is converted directly into electrical power. The operation of PEMFCs does not rely on the Carnot cycle; thus, even if they run at low temperatures ($T < 130\,^{\circ}C$) they can yield an energy conversion efficiency as high as 50% or more [1]. Furthermore, PEMFCs: (a) operate very silently and do not produce NO_x, SO_x or fine particulate; (b) yield very high power densities in very simple devices which are characterized by the lack of any mechanical moving part. Finally, when a PEMFC is fed with hydrogen the only reaction product is water; as a consequence, no greenhouse gas is dumped in the atmosphere [2]. Several of these features make this technology very friendly to the environment. For all these reasons, in the last few decades a tremendous effort has been devoted from both private companies and public institutions to the development of viable PEMFCs [3,4]. Notwithstanding that several PEMFC systems are now approaching commercialization in niche markets [5,6], the large-scale diffusion of this technology is limited by issues such as cost and durability [2,4,7]. The heart of a PEMFC is the membrane-electrode assembly (MEA), which consists in a proton-conducting membrane covered on both sides by thin electrode layers sandwiched between porous gas-diffusion electrodes. The electrode layers promote the electrochemical reactions needed for the operation of the device [8,9]. One of the most critical limitations suffered by PEMFCs is that at their low operating temperatures ($T \approx 80\,^{\circ}C$) the only viable electrocatalysts require a significant loading of platinum group metals (PGMs) [10]; ca. 1.1 g_{PGM} is reported as a requirement to obtain 1 kW [11]. In PEMFCs fuelled with hydrogen, most of the PGM loading is concentrated at the cathode, where the oxygen reduction reaction (ORR) takes place [10,12]. Therefore, the development of new ORR electrocatalysts leading to a low mass loading of PGM in the electrode configuration is a major aim in PEMFC research [10]. State-of-the-art ORR electrocatalysts used in PEMFCs consist of PGM nanoparticles, predominantly based on Pt, supported on carbon blacks with a medium surface area such as Vulcan XC-72R (Cabot Corp. TM), Ketjenblack (AkzoNobel Chemicals™) or similar furnace blacks [10,13–15]. Significant research efforts are currently devoted to improve the supports of this class of materials [16,17]. However, these systems may suffer from PGM dissolution at the highest cell operating potentials and degradation of the carbon support owing to the formation of H_2O_2 as byproduct of the ORR [7,18].

* Corresponding author. Tel.: +39 049 8275229; fax: +39 049 8275229.
E-mail address: vito.dinoto@unipd.it (V. Di Noto).
[1] Active ACS, ECS and ISE member.

0926-3373/$ – see front matter © 2011 Elsevier B.V. All rights reserved.
doi:10.1016/j.apcatb.2011.09.034

Furthermore, it is well-known that Pt-based systems are not very tolerant to poisoning effects arising from common contaminants such as halides and methanol (fuel in direct methanol fuel cells, DMFCs), which lead to a significant loss in performance [19–21]. In particular, methanol is known to permeate easily through the standard perfluorinated membranes mounted in DMFCs from the anode to the cathode compartment. Once methanol reaches the cathode it undergoes oxidation, giving so rise to a mixed potential which lowers the overall energy conversion efficiency of the DMFC [10,21]. It was suggested that one possible way to address all these issues is to prepare ORR electrocatalysts characterized by a low loading of palladium coordinated on a carbon nitride (CN) support [22]. These materials are obtained through an innovative synthetic protocol which is reasonably straightforward and, by itself, cheap. Indeed, the various preparation steps may be carried out in the open atmosphere, with simple glassware, starting from common commercial reagents, and it is easy to obtain batches of electrocatalysts in the gram range. It is not necessary to add highly purified carbon supports, and the nitrogen atoms of the CN matrix coordinate the metal atoms of the active sites, improving the tolerance of the materials to degradation in oxidizing conditions [22]. Preliminary results showed clearly that this approach is feasible, demonstrating that Pt can be substituted with the somewhat cheaper Pd in ORR electrocatalysis [22–26]. The best results were obtained with bi-metallic electrocatalysts where a metal active in the ORR such as Pd or Pt is associated with one or more co-catalytic transition metals such as Au, Co, Ni and Fe [11,22–31]. It was proposed that co-catalytic metals enhance the ORR by improving the desorption kinetics of the reaction products.

In this report, two electrocatalysts were prepared according to a new synthesis protocol which consists in the following three-step procedure: (1) synthesis of a homogeneous precursor; (2) pyrolysis of the precursor in an inert atmosphere; and (3) post-synthesis treatments and activation of ORR electrocatalysts [22,32]. To improve the tolerance of the proposed electrocatalysts towards oxidizing conditions and poisoning effects arising from chloride anions and methanol, materials with a high nitrogen concentration in the carbon nitride support matrix were devised. Two electrocatalysts are prepared and studied in detail in this report, indicated as "PdNi-CN_h 900" and "PdCoAu-CN_h 600", in an effort to achieve a better understanding of the structure–properties relationship of this family of innovative materials in systems as diverse from one another as possible [24,26]. The left side of the formulas indicates the metals included in the electrocatalysts (either Pd and Ni or Pd, Co and Au). The label –CN_h indicates that the carbon nitride support is endowed with a high concentration of nitrogen, >13 wt%. The last figure corresponds to the temperature of the pyrolysis process.

2. Experimental

2.1. Reagents

Potassium tetrachloropalladate(II) 99%, (K_2PdCl_4), potassium tetrachloroaurate(III) 98%, ($KAuCl_4$) and H_2O_2 36 vol.% are supplied by ABCR GmbH. Nickel(II) nitrate hexahydrate 99% ($Ni(NO_3)_2{\cdot}6H_2O$) is supplied by Fluka. Cobalt(II) chloride hexahydrate 98% ($CoCl_2{\cdot}6H_2O$) and polyacrylonitrile, M_w 150,000, are supplied by Aldrich. Acetonitrile and dimethylformamide are supplied by Carlo Erba. All the chemicals are used as received. XC-72R carbon black, provided as a courtesy by Carbocrom s.r.l., is washed with H_2O_2 10 vol.% prior to use. The commercial EC-20 electrocatalyst (ElectroChem Inc.) with a nominal Pt loading of 20 wt% is used as the reference without any further purification and washing procedure. In this paper, EC-20 is indicated as "Pt/C reference".

2.2. Preparation of the electrocatalysts

2.2.1. Preparation of PdNi-CN_h 900

1 mmol (326.4 mg) of K_2PdCl_4 and 1 mmol (290.8 mg) of $Ni(NO_3)_2{\cdot}6H_2O$ are dissolved in a minimum amount of milli-Q water (≈1 mL), yielding a deep red (A) and a light green (B) clear solution, respectively. 20 mL of acetonitrile is added to A and B solutions under stirring, yielding a clear red and a light green solution, respectively. A light yellow solution (C) is obtained by adding slowly and under stirring 1.6 g of polyacrylonitrile to 80 mL of dimethylformamide at about 80 °C. At this point, B and A are subsequently added dropwise to C under vigorous stirring, yielding about 120 mL of a deep red solution D whose volume is reduced to about 50 mL under stirring at about 100 °C. By adding ca. 500 mL of milli-Q water at 0 °C a soft, rubbery, amorphous dark brown material, singled out as precursor I, is obtained. This product is: (a) dried at 120 °C for 16 h in a quartz tube; (b) pyrolyzed at 300 °C for 2 h at 10^{-3} mbar. The resulting brown precursor II is then ground for 3 h in a ball mill. An aliquot of II is placed into a quartz tube and thermally treated at T_f = 900 °C for 2 h under vacuum. The product is ball-milled for 3 h, washed three times with milli-Q water, treated with H_2O_2 10 vol.% and dried under an infrared lamp. The obtained fine black powder is indicated as the PdNi-CN_h 900 electrocatalyst.

2.2.2. Preparation of PdCoAu-CN_h 600

2.1 mmol (685.5 mg) of K_2PdCl_4, 0.3 mmol (71.4 mg) of $CoCl_2{\cdot}6H_2O$, and 0.6 mmol (226.7 mg) of $KAuCl_4$ are dissolved in a minimum amount of milli-Q water (≈1 mL), yielding a deep red (A), a pink (B) and a yellow clear solution (C), respectively. 20 mL of acetonitrile is added to each solution under stirring, yielding a clear red, a light blue and a light yellow solution, respectively. A light yellow solution (D) is obtained by adding slowly and under stirring 4.78 g of polyacrylonitrile to 80 mL of dimethylformamide at about 80 °C. At this point B is added dropwise to D, which is kept under vigorous stirring yielding a dark green solution. A and C are mixed together; afterwards, the resulting solution is added dropwise under vigorous stirring to D. A dark green clear solution is obtained. The following preparation steps are identical to those already described in Section 2.2.1. The PdCoAu-CN_h 600 material is obtained by pyrolyzing the precursor at T_f = 600 °C.

2.3. Instruments and methods, electrode preparation and electrochemical measurements, preparation of membrane-electrode assemblies and tests in a single-cell configuration

The detailed information concerning these issues is reported elsewhere [28,33–45] and in Supplementary information.

3. Results

3.1. Chemical composition of the electrocatalysts

The chemical analysis of the proposed electrocatalysts is reported in Table 1(a). It is observed that the preparation procedure yields electrocatalysts characterized by a nitrogen content larger than 13 wt%. With respect to PdNi-CN_h 900, the chemical composition of PdCoAu-CN_h 600 includes a small amount of hydrogen and more nitrogen. This evidence points to an incomplete graphitization of the carbon nitride support in PdCoAu-CN_h 600, attributed to the lower temperature of the pyrolysis process (see Section 2.2). It should be observed that: (a) the molar ratio of the metal atoms in the electrocatalysts is quite similar to that in the composition of the reagents; and (b) despite the extensive washing and the activation procedure, the electrocatalysts include a significant amount of potassium. This latter evidence is attributed to an incomplete

Table 1
Composition parameters of PdNi-CN_h 900 and PdCoAu-CN_h 600.

(a) Bulk chemical composition

Product	wt%								Formula
	Pd[a]	Ni[a]	Co[a]	Au[a]	K[a]	C[b]	N[b]	H[b]	
PdNi-CN_h 900	1.87	0.77	–	–	0.70	66.19	13.87	–	$K_{1.02}[PdNi_{0.75}C_{314}N_{56}]$
PdCoAu-CN_h 600	3.77	–	0.21	1.97	1.99	52.16	18.06	0.48	$K_{1.44}[PdCo_{0.10}Au_{0.33}C_{123}N_{33}H_{13}]$

(b) TG analysis of the proposed electrocatalysts and of the Pt/C reference. Measurements are collected in oxidizing atmosphere

Product	% of mass loss at 200 °C	T_{ME} (°C)[c]	ΔW_{ME} (wt%)[c]	Residue (wt%)[d]
PdNi-CN_h 900	7.2	449	82.7	8.2
PdCoAu-CN_h 600	6.5	458	79.8	12.8
Pt/C reference	1.9	403	63.2	20.7

(c) Surface chemical composition (atom%) of proposed electrocatalysts and reference as measured using XPS

Product	Element								
	Pt	Pd	Ni	Co	Au	K	C	N	O
PdNi-CN_h 900	–	0.35	0.31	–	–	0.49	70.45	8.50	19.87
PdCoAu-CN_h 600	–	0.34	–	0.41	0.10	0.51	68.98	15.23	14.43
Pt/C reference	1.1	–	–	–	–	–	93.8	–	5.1

[a] Determined by ICP-AES spectroscopy.
[b] By elemental analysis.
[c] T_{ME} and ΔW_{ME} are the temperature and the value of mass elimination.
[d] Residue determined between 550 and 700 °C in Fig. 1(b).

reduction of the metal complexes during the pyrolysis process. It is expected that a significant fraction of metal atoms is included in the electrocatalysts as anionic complexes, whose electric charge is counterbalanced by potassium cations [31].

3.2. Thermogravimetric analyses

The thermogravimetric (TG) profiles of the proposed electrocatalysts are shown in Fig. 1. The parameters determined from TG profiles, collected under air oxidizing atmosphere, are reported in Table 1(b). With respect to the Pt/C reference, both the proposed materials show a higher mass loss at temperatures <200 °C (see Fig. 1 and Table 1(b)), which corresponds to water or loosely bound organic compounds adsorbed on the surface of the CN electrocatalysts. This evidence is consistent with a more hydrophilic surface in CN systems with respect to the Pt/C reference. The TG profiles in N_2 atmosphere clearly show that, with respect to the Pt/C reference, both CN electrocatalysts are less tolerant towards thermal decomposition at $T > 700$ °C (see Fig. 1(a)). This result is ascribed to the incomplete graphitization of the CN supports of the electrocatalysts. In detail, PdCoAu-CN_h 600 is less stable than PdNi-CN_h 900. Indeed, PdCoAu-CN_h 600 undergoes a pyrolysis process at a lower temperature. Thus, a lower degree of graphitization is expected in this material. The TG profiles collected under oxidizing atmosphere clearly indicate that, with respect to the Pt/C reference, the main decomposition event of both CN electrocatalysts is shifted at temperature values higher by ca. 50 °C (see Fig. 1(b)); the supports of both PdNi-CN_h 900 and PdCoAu-CN_h 600 are stable up to ca. 400 °C. The main decomposition event is assigned to the oxidation of the graphitic-like support of CN materials and the shift is attributed to the high nitrogen concentration present in the support of the electrocatalysts. It is expected that this latter feature stabilizes both materials by strengthening the interactions between the support and the metal-rich active sites. In addition, the coordination of the active sites of the electrocatalysts with nitrogen ligand groups inhibits the formation of metal oxides, which are expected to promote the degradation of the graphitic matrix at high temperature. Taken together, with respect to the Pt/C reference the CN electrocatalysts are more tolerant towards oxidative decomposition. It should be observed that the high-temperature residues detected in TG profiles measured under oxidizing atmosphere are consistent with the total amount of metals determined through ICP-AES analyses (see Table 1(a) and (b)). The residues thus determined are expected to consist of nonvolatile metal oxides or other

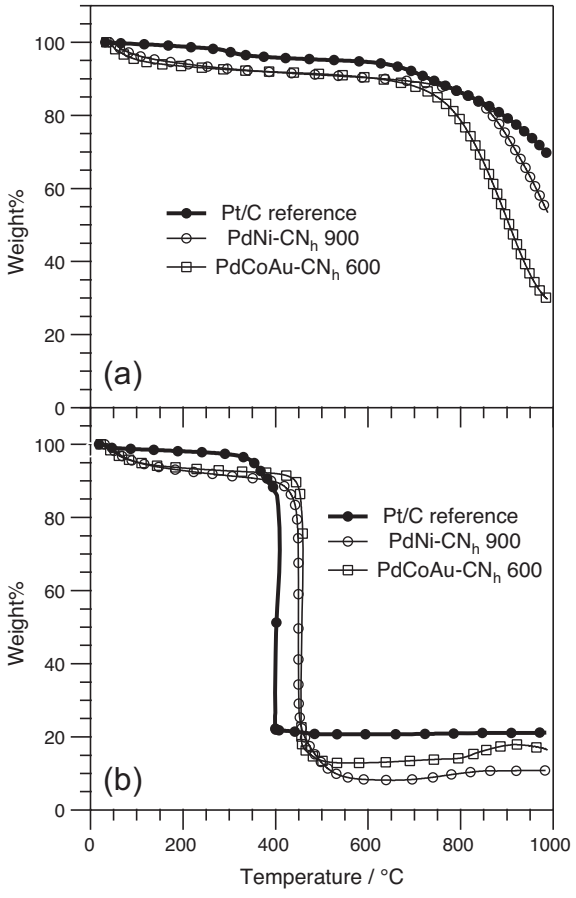

Fig. 1. TG profiles of electrocatalysts: (a) measured under N_2 atmosphere and (b) measured under air oxidizing atmosphere.

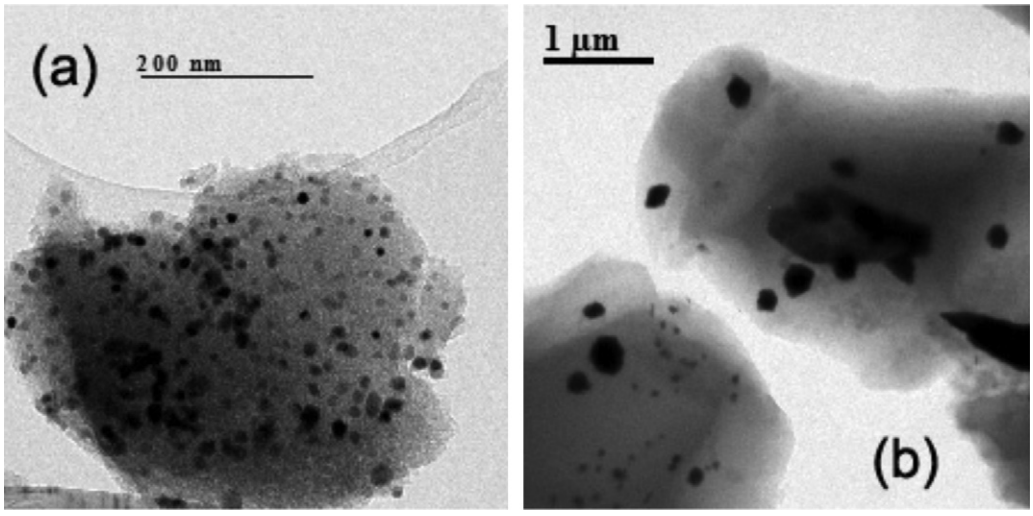

Fig. 2. HR-TEM images of electrocatalysts. (a) PdNi-CN_h 900 and (b) PdCoAu-CN_h 600.

carbon or nitrogen derivatives. Finally, at $T > 700\,^{\circ}C$ a significant mass increase is detected in the TG profiles (~2–4%) which, in accordance with previous studies on materials including cobalt [23], corresponds to the progressive adsorption of oxygen by the residues.

3.3. Morphology studies and surface analysis

3.3.1. High-resolution transmission electron microscopy

The HR-TEM images of the proposed electrocatalysts are shown in Fig. 2. It is observed that the proposed electrocatalysts present metal-rich phases supported on the CN matrix. PdNi-CN_h 900 is characterized by a single metal-rich phase featuring grains whose average size is lower that 30 nm, whereas in PdCoAu-CN_h 600 two metal-rich phases are detected; the former shows grains whose average size is lower that 30 nm, while the latter is characterized by a size $d > 200$ nm. The morphology of the electrocatalysts includes ORR active sites supported on the surface of the metal-rich domains. It should be observed that this morphology is very similar to that revealed in the literature [22] for similar carbon nitride-based systems with a high activity in the ORR process.

3.3.2. X-ray photoelectron spectroscopy

XPS studies are carried out to obtain information on the composition and the chemical species present on the surface of the CN electrocatalysts. Fig. 3 reports the survey spectra of the Pt/C reference, PdCoAu-CN_h 600 and PdNi-CN_h 900. As expected, O and C are detected in all the samples. Pd is found in both PdCoAu-CN_h 600 and PdNi-CN_h 900; Pt is revealed in the Pt/C reference. PdCoAu-CN_h 600 shows a weak peak ascribed to gold. In all the samples, the binding energy of the C peak is 284.4 eV, which corresponds to the typical BE value of graphitic-like materials and clearly shows that the samples do not undergo charging effects [43]. A significant amount of nitrogen is detected in both PdCoAu-CN_h 600 and PdNi-CN_h 900, revealing that this element is also present in the surface layers of the nanoparticles. A very small amount of chlorine is evidenced in the PdCoAu-CN_h 600 sample which, in agreement with other studies [28], highlights that oxidized metal species are still found in the final material. To carry out quantitative analyses, detailed scans are acquired for the C1s, O1s, N1s, Co2p, Ni2p, Pd3d, Au4f and Pt4f regions; results are listed in Table 1(c). Fig. 4(a1) and (b1) shows the decomposition of the Pd3d spectral region of PdNi-CN_h 900 and PdCoAu-CN_h 600 electrocatalysts, respectively. In the spectral profile of PdNi-CN_h 900 only one doublet of peaks is revealed and is ascribed to Pd(II) species (see Fig. 4(a1)). PdCoAu-CN_h 600 (see Fig. 4(b1)) shows two doublets peaking at ca. 335 and 337.8 eV, which are ascribed to Pd(0) and Pd(II) metal species, respectively [23]. Co and Ni show only one component, which is ascribed to metal oxidized species, whereas for Au only one peak is detected, corresponding to Au(0). The Pt4f region of the Pt/C reference evidences only one spectral feature peaking at 71.5 eV, which is typical of a Pt(0) specie. The XPS profiles of the N1s region of the proposed CN electrocatalysts are decomposed as shown in Fig. 4(a2) and (b2). One component peaking at ca. 400 eV is detected in both PdNi-CN_h 900 and PdCoAu-CN_h 600, attributed to the N of the CN matrix. PdCoAu-CN_h 600 features one additional component at ca. 398 eV, ascribed to the cyanide terminal groups not merged into the graphitic-like CN matrix. The two spectral features located at ca. 284.4 and 286 eV correspond to C1s peaks of PdNi-CN_h 900 and PdCoAu-CN_h 600 samples. The peak at 284.4 eV corresponds to carbon atoms incorporated in graphitic CN layers, whereas the feature at 286 eV is attributed to the carbon atoms of functionalized groups with a higher electronegativity such as those based on nitrogen and oxygen deriving from an incomplete graphitization of the CN matrix. The symmetric O1s XPS peaks of PdNi-CN_h 900 and PdCoAu-CN_h 600 are both measured at 532 eV. This feature is typical of surface oxygenated groups such as carboxylates, alcoholates, phenols, polyalcohol and polyether functionalities [29].

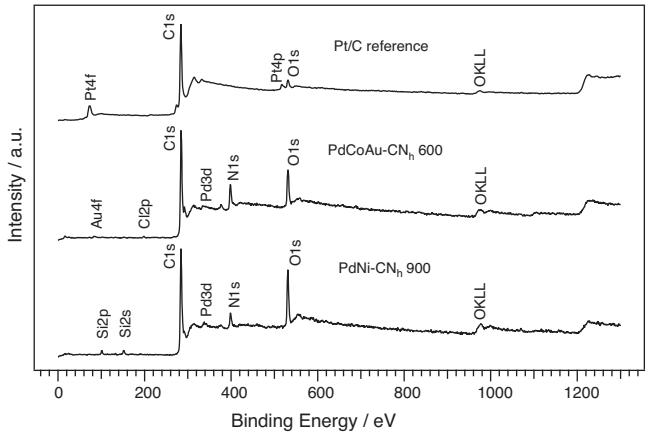

Fig. 3. Survey XPS spectra of the electrocatalyst materials.

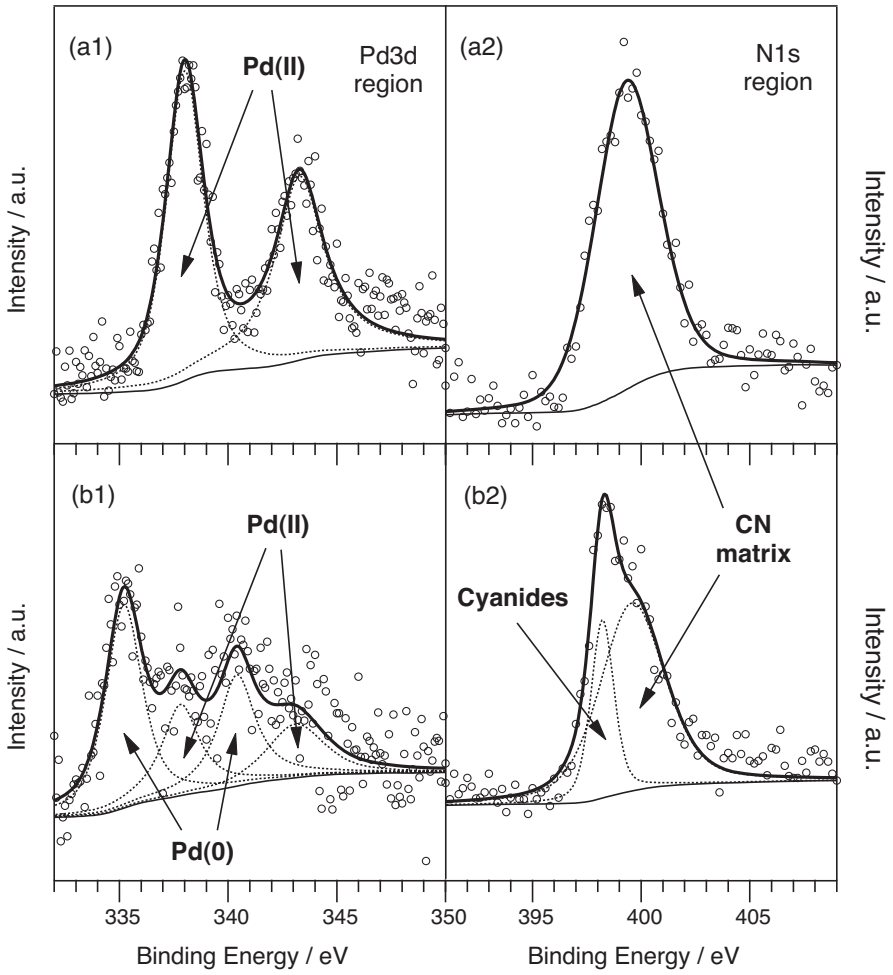

Fig. 4. Decomposition of selected regions of the XPS spectra of the proposed electrocatalysts. The label (*xy*) is read as follows: *x* = a, b for PdNi-CN_h 900 and PdCoAu-CN_h 600, respectively; *y* = 1, 2 for the Pd3d and the N1s region, respectively.

The detailed spectra of Co, Ni, Au, Pt, C and O are reported in Supplementary information.

3.4. Structural studies

3.4.1. Vibrational spectroscopy

Structural information on PdNi-CN_h 900 and PdCoAu-CN_h 600 electrocatalysts is determined by Fourier-transform infrared spectroscopy in the far (FT-FIR) and in the medium (FT-MIR) IR regions, and by μ-Raman spectroscopy. The profiles of μ-Raman, FT-MIR and FT-FIR spectra are shown in Fig. 5. The correlative assignments of vibrational peaks are listed in Table 2 [29,46–48]. The following main structural features are clearly evidenced in the vibrational spectra: (a) bands deriving from the CN backbone; (b) peaks associated to the vibrational modes of oxygenated functional groups located on the surface of the CN particles; (c) metal–ligand peaks associated with the vibrations of metal species constituting the active electrocatalytic sites of CN-based materials. In the range between 1000 and 1700 cm^{-1}, the FT-MIR and μ-Raman spectra clearly evidence the typical vibrational modes associated with graphitic-like materials. In detail, the bundle of peaks whose main components are located at ca. 1350 and 1590 cm^{-1} are typical vibrational modes of graphitic-like CN structures with a nitrogen content lower than 20 wt% [29]. Further insight on the structural features of the proposed electrocatalysts is obtained by analyzing the μ-Raman spectra. The latter are decomposed by a maximum of four Lorentzian peaks, located at ca. 1200, 1350, 1520 and 1590 cm^{-1}. The peaks at 1350 and 1590 cm^{-1} are attributed to the A_{1g} mode of lattice vibration (D band) and to the E_{2g} graphitic band (G band), respectively. In a perfect graphitic lattice only the latter band is Raman-active. The A_{1g} mode of lattice vibration (D band) becomes Raman-active owing to the disorder in the system, which can be due both to the finite dimensions of the CN particles, or to the substitution of carbon atoms with nitrogen atoms in the CN matrix. An increasing degree of structural disorder is associated with a decreasing value of the ratio between the intensities of the G and the D bands (I_G/I_D ratio) [47,49]. Fig. 5 evidences clearly that the I_G/I_D ratio is similar for the Pt/C reference and the PdNi-CN_h 900 material (see Fig. 5(a1) and (b1), respectively). On the other hand, with respect to the PdCoAu-CN_h 600 material, the I_G/I_D ratio for the Pt/C reference is significantly larger. This evidence is interpreted admitting that the disorder of the graphitic-like CN structure increases in the order: Pt/C reference ≈ PdNi-CN_h 900 < PdCoAu-CN_h 600. In the Pt/C reference, the structural disorder arises from the finite dimensions of the particles of the graphitic support [29]. In the PdNi-CN_h 900 electrocatalyst, the graphitization of the CN support triggered by the pyrolysis process is essentially complete, yielding a system characterized by a structural disorder quite similar in comparison with that of the graphitic support of the Pt/C reference. With respect to PdNi-CN_h 900, the higher structural disorder of the PdCoAu-CN_h 600 electrocatalyst is a consequence of the incomplete graphitization of the CN support arising from the lower temperature of the final pyrolysis process (see Section 2.2). In particular, in PdCoAu-CN_h 600 a

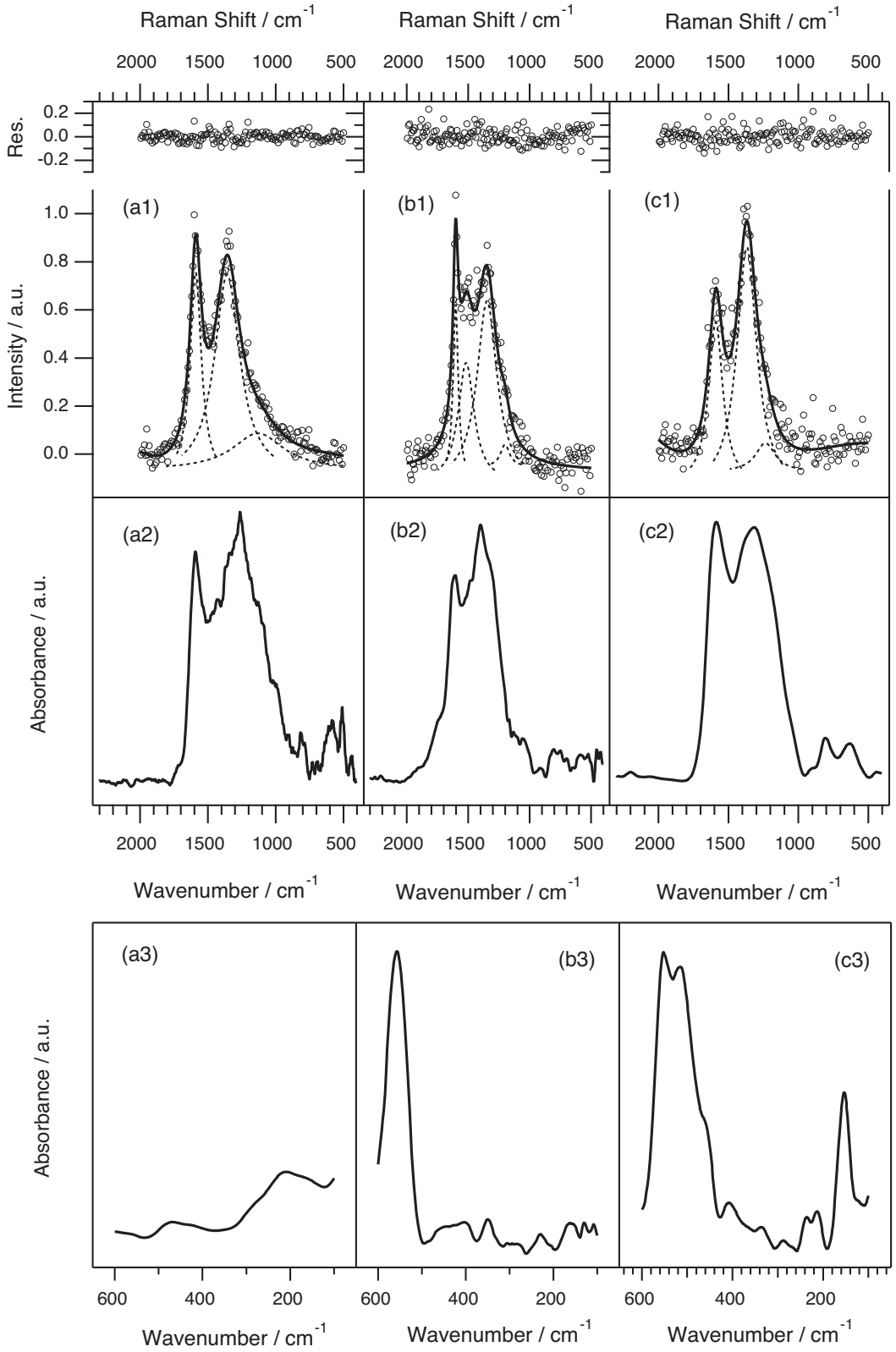

Fig. 5. Vibrational spectroscopy spectra of the proposed electrocatalysts. The label (*xy*) is read as follows: *x* = a, b, c for the Pt/C reference, PdNi-CN_h 900 and PdCoAu-CN_h 600 materials, respectively; *y* = 1, 2, 3 for μ-Raman, FT-MIR and FT-FIR spectra, respectively.

significant source of structural disorder is expected to be the incomplete inclusion of nitrogen atoms in the graphene layers of the CN support, in accordance with the XPS studies (see Section 3.3.2). The Lorentzian peak at ca. 1520 cm^{-1} in the μ-Raman spectrum of the PdNi-CN_h 900 electrocatalyst is attributed to an amorphous CN phase at the interface between different graphitic-like CN particles of the support [47]. In accordance with other FT-MIR analyses [29], the broad Lorentzian peak located in the μ-Raman spectrum

Table 2
MIR, FIR, Fourier-transform IR (FT-IR), and μ-Raman band assignments of electrocatalyst and reference materials.

Pt/C reference[a]		PdNi-CN_h 900[a]		PdCoAu-CN_h 600[a]		Band Assignment[b, c]	Reference
IR	Raman	IR	Raman	IR	Raman		
1710 (sh, w)		1734 (sh, w)				ν(COO)	[46]
1588 (vs)	1590 (vs)	1602 (vs)	1603 (vs)	1590 (vs)	1591 (vs)	G-band in-plane stretching: a) IR E_{2u}; b) Raman E_{2g}	[29]
			1518 (m)			Amorphous carbon	[47]
1430 (w)		1400 (vs)		1400 (sh, s)		A_{2u}	[29]
1327 (w)	1358 (s)	1323 (sh, s)	1347 (s)	1323 (vs)	1368 (s)	D-band, A_{1g} longitudinal acoustic wave	[29]
1258 (vs)						ν(CO), ether	[29]
	1131 (vw, b)		1200 (vw, b)		1235 (vw, b)	ν(CO) modes	[29]
1115 (vw)		1120 (w)		1140 (sh, m)		ν(CO), phenolic	[29]
1020 (sh, vw)		1025 (w)		1030 (sh, w)		ν(CO), alcoholic	[29]
800 (w)		796 (vw)		800 (w)		A_{2u} (oop)	[29]
				629 (w)			
		552 (s)		550 (s)		ν(Pd-O)	[48]
				514 (s)		ν(Pd-N)	[48]
470 (w)						ν(Pt-C)	[48]
				453 (sh, m)		ν(Co-O)	[48]
420 (w)						oop bending mode	[29]
		404 (vw)		407 (vw)		ν(Pd-O)	[48]
		349 (vw)				ν(Ni-O)	[48]
				337 (vw)		ν(Co-O)	[48]
				234 (vw)		Graphitic A_g lattice vibrations	[29]
215 (vw)		230 (vw)		213 (vw)			
				153 (m)		ν(Pd-Cl)	[48]

[a]Relative intensities are reported in parentheses: vs, very strong; s, strong; m, medium; w, weak; vw, very weak; sh, shoulder; b, broad.
[b]ν, stretching; oop, out-of-plane.
[c]Assignments performed correlatively on the basis of [29,46–48].

at ca. 1200 cm^{-1} is attributed to the ν(CO) stretching modes. This peak is centered at 1235, 1200 and 1131 cm^{-1} for PdCoAu-CN_h 600, PdNi-CN_h 900 and the Pt/C reference, respectively (see Table 2). In detail, these ν(CO) vibrational modes are associated mainly to the ether and phenol functional groups located on the surface of the nanoparticles composing the CN matrix [29]. The shift of ν(C–O) mode to lower wavenumbers witnesses that the contribution of phenol functional groups is increased as the graphitization process of the support approaches completion. The presence on the surface of the CN support nanoparticles of such oxygen-based functional groups (alcohols, ethers and phenols) is further supported by the modes in the FT-MIR spectral region between 1000 and 1260 cm^{-1} (see Fig. 5(a2), (b2) and (c2)). These results are consistent with the literature [29] and with the results of the XPS analysis (see Section 3.3.2). The inspection of the FT-FIR spectra at frequencies lower than 700 cm^{-1} evidences several metal–ligand stretching vibrations including ν(Pd–N), ν(Pd–O), ν(Pd–Cl), ν(Ni–O) and ν(Co–O) [48]. Modes ascribed to the A_g vibration of the graphitic lattice are observed at ca. 220 cm^{-1} in both CN electrocatalysts and in the Pt/C reference (see Fig. 5(a3), (b3) and (c3)). Weak vibrational modes attributed to ν(Ni–O) and ν(Co–O) are revealed for PdNi-CN_h 900 and PdCoAu-CN_h 600, respectively. ν(Pd–O) modes are detected in both PdNi-CN_h 900 and PdCoAu-CN_h 600 (see Fig. 5(b3) and (c3), respectively). In addition, the FT-FIR spectrum of the PdCoAu-CN_h 600 electrocatalyst reveals modes at 514 and 153 cm^{-1} attributed to ν(Pd–N) and ν(Pd–Cl) vibrations, respectively. In PdNi-CN_h 900 no Pd–Cl and Pd–N vibrational modes are detected, probably owing to the high temperature of the pyrolysis process. This behaviour is consistent with results reported elsewhere [22]. The presence of metal–oxygen vibrational modes could be ascribed to two processes: (a) the activation of the materials with oxidants such as hydrogen peroxide; and (b) the incomplete graphitization of the CN matrix.

3.4.2. *Powder X-ray diffraction*

The structural features of PdNi-CN_h 900 and PdCoAu-CN_h 600 are studied by powder X-ray diffraction. The XRD profiles of the proposed electrocatalysts and of the Pt/C reference are shown in Fig. 6. The XRD peaks of the Pt/C reference are easily Miller-indexed on the basis of previous studies [29,50,51], revealing the typical features of graphite (peak at $2\theta \approx 25^\circ$, attributed to the (0 0 2) reflection) and of platinum nanocrystals with a fcc structure, located at $2\theta \approx 39.9^\circ$, 46.1°, 67.6°, 81.6° and 85.9°, which are assigned respectively to the (1 1 1), (2 0 0), (2 2 0), (3 1 1) and (2 2 2) interplanar distances. The XRD profiles of PdNi-CN_h 900 and PdCoAu-CN_h 600 show a broad peak at $2\theta \approx 25.2^\circ$, which corresponds to the (0 0 2) reflection of the graphitic-like carbon nitride matrix. The XRD spectrum of PdNi-CN_h 900 shows very weak intensities at $2\theta \approx 40.2^\circ$ and 46.8°, which are ascribed to the (1 1 1) and (2 0 0) reflections of a palladium-based fcc phase. The XRD spectrum of PdCoAu-CN_h 600 is characterized by strong reflections at $2\theta \approx 39.5^\circ$, 45.8°, 66.6°, 80.3° and 84.5°, assigned respectively to the (1 1 1), (2 0 0),

(2 2 0), (3 1 1) and (2 2 2) reflections of two palladium-based fcc phases. Weaker, sharp peaks are evidenced at $2\theta \approx 28.4^\circ$, 35.1°, 36.7°, 40.8°, 42.8° and 51.7°. The XRD profiles of the proposed materials are studied by Scherrer analysis, carried out on the peak at $2\theta \approx 25^\circ$. A very small crystal size ($d \approx 2$ nm) is determined for the support phase of all the investigated materials. The Rietveld analysis, carried out on the XRD spectra [44], allows the identification of the structural parameters of the metal-rich phases, summarized in Table 3. It is also observed that the crystallite size of the metal-rich phases is consistent with that of the metal-rich domains evidenced by HR-TEM (see Fig. 2). The inset of Fig. 6 shows the decomposition by the Rietveld method of the XRD spectra in the region corresponding to the (1 1 1) and (2 0 0) reflections of the fcc phases of the PdNi-CN_h 900 electrocatalyst. It is observed that the latter is characterized by two metal-rich phases. The first phase is associated to the sharp XRD peaks, essentially corresponding to the palladium–nickel alloy with composition $Pd_{20}Ni_{0.54}$. The second phase, which consists of smaller nanocrystals, corresponds to a palladium–nickel alloy with a higher atomic ratio of nickel, $Pd_{20}Ni_{5.64}$. In addition, a broad reflection is detected at $2\theta \approx 44^\circ$, overlapped in the same region to the spectral profiles of the other phases. The reflection is ascribed to the (1 0 0) and (1 0 1) reflections of a graphitic-like CN support. PdCoAu-CN_h 600 is characterized by two main metal-rich phases, associated to palladium–gold alloys with $Pd_{20}Au_{13}$ and $Pd_{20}Au_{3.3}$ stoichiometries, which include traces of cobalt atoms. It should be observed

Table 3
Main features of the metal-rich phases [44].

Product	Phase[a]	Relative (wt%)	Crystallite size (nm)[e]
PdNi-CN_h 900	$Pd_{20}Ni_{0.54}$[b]	27	23.6
	$Pd_{20}Ni_{5.64}$[b]	73	4.7
PdCoAu-CN_h 600	$Pd_{20}Au_{13}$[c]	19	19.9
	$Pd_{20}Au_{3.3}$[c]	81	18.4
Pt/C reference	Pt[d]	100	3.0

[a] Approximate stoichiometry determined from Vegard's law.
[b] Starting phases: Pd → fcc lattice, S.G. Fm3m, a = 3.889 Å, #05-0681 PCPDF database; Ni → fcc lattice, S.G. Fm3m, a = 3.523 Å, #04-0850 PCPDF database.
[c] Starting phases: Pd → fcc lattice, S.G. Fm3m, a = 3.889 Å, #05-0681 PCPDF database; Au → fcc lattice, S.G. Fm3m, a = 4.064 Å, #01-1174 PCPDF database.
[d] Pt → fcc lattice, S.G. Fm3m, a = 3.911 Å, #87-0640 PCPDF database.
[e] Determined using the Scherrer method on the $I_{1\,1\,1}$ reflections and corresponding to the average crystallite dimension along the reflecting plane (1 1 1).

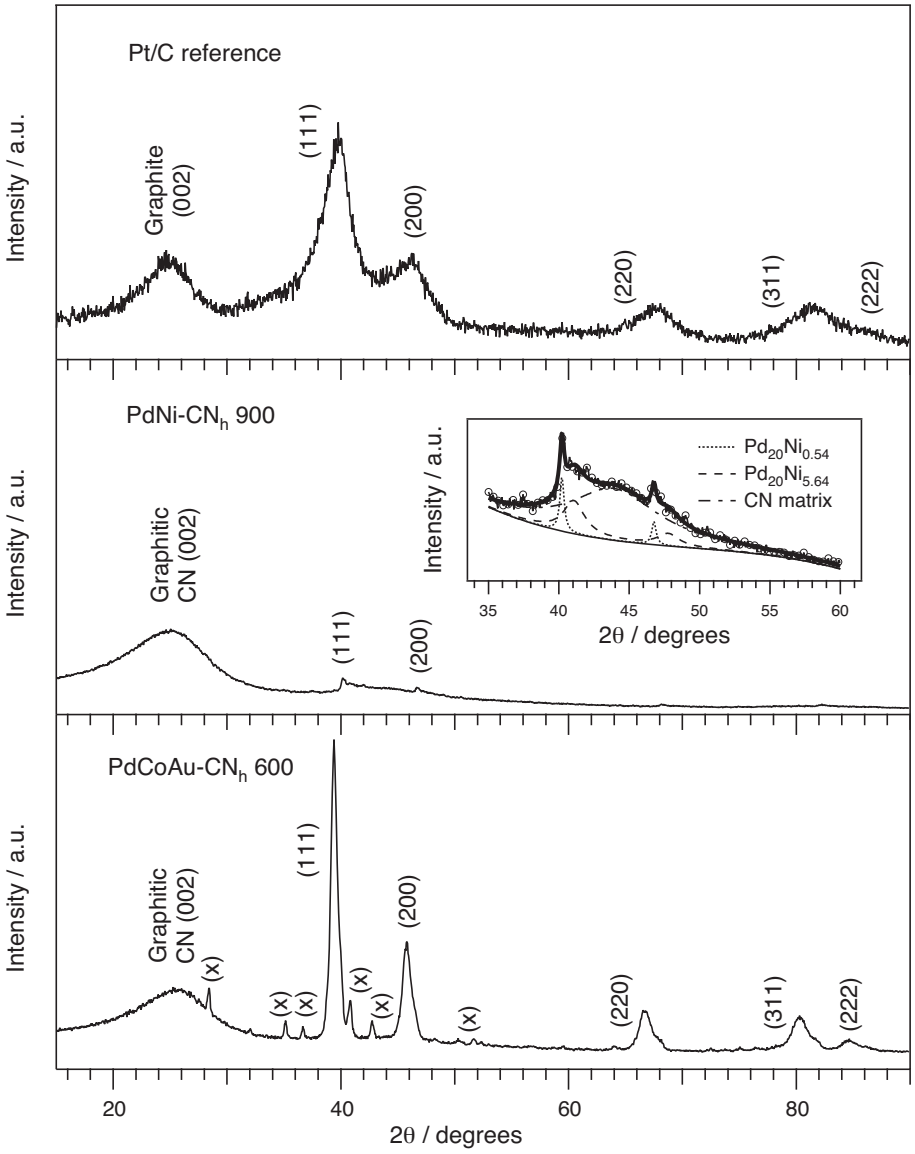

Fig. 6. Powder XRD patterns of the proposed electrocatalysts and of the Pt/C reference. The main reflections of fcc phases are indexed. (x) marks the reflections of the non identified phase (phases).

that the Co/Pd and Co/Au atomic ratios are equal to ca. 0.1 and 0.3, thus Co atoms were not included explicitly in the stoichiometry of the two alloys.

3.5. Structural and morphological hypothesis of electrocatalysts

The results discussed above allow to draw a coherent picture of the structural features characterizing PdNi-CN_h 900 and PdCoAu-CN_h 600 electrocatalysts, which consist of polycrystalline CN particles of size >100 nm embedding crystalline metal-rich domains. PdNi-CN_h 900 and PdCoAu-CN_h 600 electrocatalysts are obtained by pyrolysis processes from homogeneous precursors. The temperature of the pyrolysis processes is a crucial parameter to consider in order to modulate the structural features of materials [22]. One of the most important effects of the pyrolysis process is the phase segregation between the CN matrix and the metal-rich phases (MRP). The MRP domains are randomly distributed inside the CN matrix (see Fig. 2). As expected, the chemical composition of the precursor has a profound effect on the morphology of the MRP domains. With respect to PdNi-CN_h 900, PdCoAu-CN_h 600 is characterized by larger size of the MRP domains. This is probably due to the presence of gold which, owing to its tendency to be easily reduced in the CN matrix, can probably facilitate the segregation processes of the MRP even at low temperatures. Indeed, as the temperature is raised, Au develops more than one stable alloy with palladium (data not shown). The analysis of the powder XRD diffraction patterns of PdNi-CN_h 900 allows to detect large crystals based on almost pure palladium. However, it should be highlighted that Pd is present mostly as very small crystals of Pd–Ni alloys ($d \approx 5$ nm). This phenomenon can be explained considering that the palladium-based phases are not stable at 900 °C in the presence of carbon, nitrogen and nickel atoms. Furthermore, it is hypothesized that in this condition amorphous phases, which are not detected by powder XRD spectra, could be gradually formed, thus reducing the size of the Pd crystalline nanoparticles. Indeed, bulk ICP-AES analysis evidences a Pd:Ni molar ratio ρ equal to ca. 1:0.75, whereas the XRD analysis detected a value for ρ close to 1:0.2. Therefore, it is suggested that the difference in ρ arises from the inclusion of Ni atoms in the CN matrix. The latter phase could be attributed to highly disordered graphitic-like carbon nitride domains, which form large polycrystalline particles with $d > 100$ nm. This hypothesis is supported by μ-Raman, powder XRD studies and HR-TEM micrographs. In details, the structural features of the CN support, detected by μ-Raman and powder XRD spectra, are corresponding to those of a CN matrix where some sp^2 carbon atoms of the graphene layers were replaced by nitrogen, as it was already observed in similar carbon nitride materials characterized by a CN matrix whose stoichiometry includes a few wt% of nitrogen [11,22,26,24,29]. PdCoAu-CN_h 600 is characterized by a poorer incorporation of nitrogen atoms in its CN matrix in comparison with PdNi-CN_h 900, even if the latter electrocatalyst includes a smaller concentration of nitrogen atoms in its chemical composition (see Table 1(a)). This observation is supported by the analysis of the G-band in the μ-Raman spectrum, which is characterized by a frequency increase going from PdCoAu-CN_h 600 to PdNi-CN_h 900 ($1597\ cm^{-1} < 1604\ cm^{-1}$). It should be observed that: (a) the G peak in the nitrogen-free Pt/C reference is revealed at $1589\ cm^{-1}$; (b) as witnessed by the μ-Raman studies, the CN matrix of PdNi-CN_h 900 is more graphitic-like than that of PdCoAu-CN_h 600. Furthermore, both powder X-ray diffraction and μ-Raman investigations point to electrocatalysts where the long-range order in the bulk materials is limited at most to a few nanometers. Moreover, as revealed by HR-TEM images (see Fig. 2), each CN domain presents a significantly larger size. In addition, the stoichiometry and the TG results suggest that as the temperature of the pyrolysis process is raised: (a) the graphitization process of the CN matrix approaches completion; and (b) the segregation between the metal-rich phases and the CN matrix becomes more and more pronounced as evidenced by the disappearance of Pd–N vibrational mode in the FT-FIR spectra of PdNi-CN_h 900 (see Table 2).

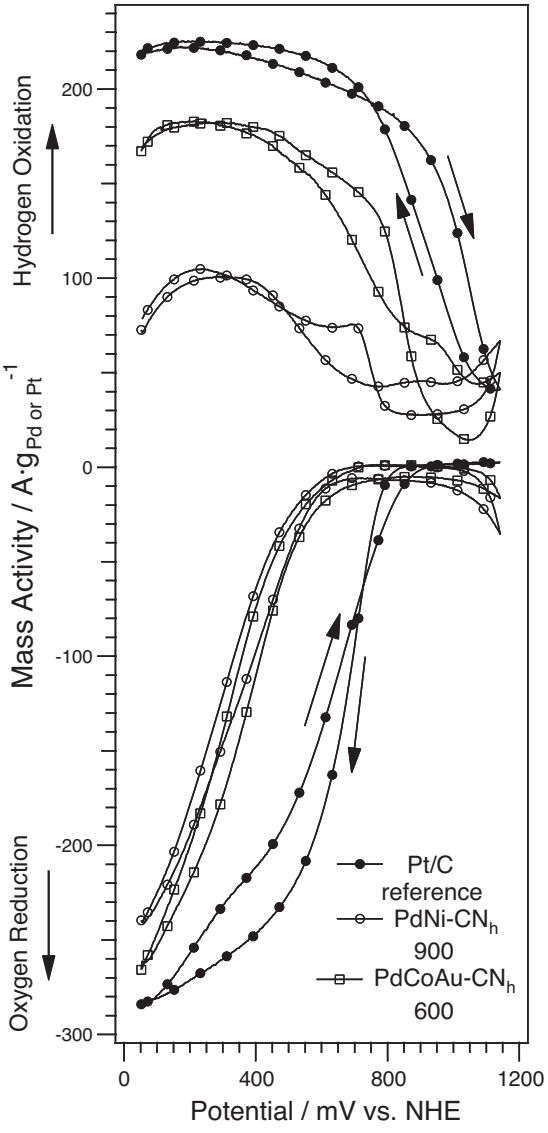

Fig. 7. CV-TF-RDE profiles of the Pt/C reference and the synthesized materials in either a pure oxygen or in a pure hydrogen atmosphere after correction from the contributions due to the capacitive currents [26]. 5 mV s^{-1}, 1600 rpm, 60 °C, $HClO_4$ 0.1 M.

3.6. Electrochemical studies

3.6.1. Determination of ORR performance

The electrochemical performance of PdNi-CN_h 900 and PdCoAu-CN_h 600 in the ORR and in the HOR is studied by the CV-TF-RDE method as shown in Fig. 7. The CV profiles in the ORR are corrected for the capacitive and mass transport contributions as described in the literature [26,31,52] and are subsequently elaborated to obtain the Tafel plots shown in Fig. 8(a). Fig. 8(b) reports the Levich–Kuotecky plots of the materials both in the ORR and in the HOR. It is observed that, with respect to the Pt-based reference, the ORR overpotentials of the PdNi-CN_h 900 and PdCoAu-CN_h 600 are ca. 250 and 200 mV higher, respectively. The Tafel slope of the ORR increases for all the materials from values of about 60–90 mV $decade^{-1}$ to ca. 120 mV $decade^{-1}$ as the current

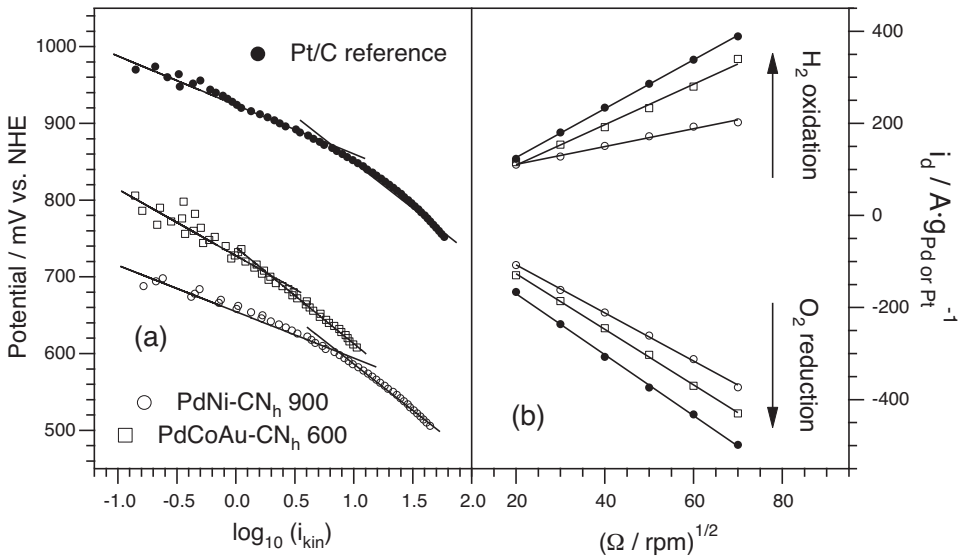

Fig. 8. (a) Tafel plots and (b) Levich–Kuotecky plots of the proposed materials determined from CV-TF-RDE profiles reported in Fig. 7. The correction to the Tafel plots due to mass transport is carried out setting as i_d the values of the ORR profiles at $V = 0.05$ V vs. NHE. All the data are corrected removing the contributions due to capacitive currents [26].

density is raised. This behaviour is typical of electrocatalysts where the ORR is carried out on PGMs through the four-electron mechanism [22,31,53,54]. In the region at the lowest current density, with respect to the Pt/C reference and to the PdNi-CN$_h$ 900, the Tafel slope of the PdCoAu-CN$_h$ 600 electrocatalyst is the highest, probably owing to a lower surface oxide coverage of active sites. This effect is likely associated to the presence of gold atoms in the material, which are known to promote the reduction of neighbouring Pd atoms to Pd(0) [55,56]. Fig. 8(b) clearly shows that with respect to the Pt/C reference, the proposed electrocatalysts are characterized by very similar Levich slopes in the ORR. This evidence is consistent with a very similar reaction mechanism in the ORR in the low-potential region for all the investigated materials [22]. Fig. 7 shows that in the HOR the maximum mass activity decreases in the order Pt/C reference > PdCoAu-CN$_h$ 600 > PdNi-CN$_h$ 900 with values of ca. 220, 185 and 100 A $g_{Pd,\,Pt}^{-1}$, respectively. In addition, the Levich slopes in the HOR increase in the order PdNi-CN$_h$ 900 < PdCoAu-CN$_h$ 600 ≤ Pt/C reference. These results indicate that the mass transport of H_2 towards the active sites improves in the order PdNi-CN$_h$ 900 < PdCoAu-CN$_h$ 600 < Pt/C reference, thus demonstrating that the pyrolysis process and the electrocatalyst metal combination is crucial in the modulation of the electrocatalytic performance of the materials which results higher for the sample with the highest porosity, i.e., PdCoAu-CN$_h$ 600. Thus, the HOR performance of PdNi-CN$_h$ 900 is significantly lower than that of PdCoAu-CN$_h$ 600 and of the Pt/C reference.

3.6.2. *Effect of methanol and chloride anions on the ORR*

Fig. 9(a1), (b1) and (c1) shows the effect of methanol on the performance in the ORR of the proposed materials. It is observed that the Pt/C reference is significantly affected by the presence of methanol (see Fig. 9(a1)). Indeed, on rising the CH_3OH concentration the ORR overpotential increases and the intensity of a broad and positive peak rises, which is ascribed to the oxidation of methanol on platinum active sites. It should be highlighted that the influence of methanol poisoning in the ORR on both PdNi-CN$_h$ 900 and PdCoAu-CN$_h$ 600 is essentially negligible. The effect in the ORR process of chloride contamination is shown in Fig. 9(a2), (b2) and (c2). A significant increase in the ORR overpotential of the platinum active sites of the Pt/C reference is observed on raising the Cl^- concentration in the electrolyte (see Fig. 9(a2)). At $[Cl^-] = 10^{-2}$ M, the ORR overpotential of the Pt/C reference increases by 160 mV, whereas in both PdNi-CN$_h$ 900 and PdCoAu-CN$_h$ 600 a lower effect is revealed, with values of ca. 75 and 45 mV, respectively.

3.7. *Single fuel cell performance*

The cathodic electrode layers of all the investigated MEAs are formulated maintaining constant the loading of both the catalytic mixture and of the Nafion® ionomer (up to a total of ∼7 mg cm^{-2}). This is done to maintain constant the losses arising both from the water management and from the mass transport phenomena of both reagents and products. Since the PGM concentration in the electrocatalysts depends on the material (see Table 1(a)), the cathodes of the MEAs necessarily include a different loading of PGMs. Thus, for the sake of comparison, the normalization of the cell currents to the cathodic PGM mass (i.e., the "mass activity") is of crucial importance in order to study the performance of the proposed materials. The single cell Tafel plots shown in Fig. 10(a1), (b1) and (c1) are determined as described elsewhere [22,45] from the polarization curves of single PEMFCs collected near open-circuit potential (OCP). The dependence of Tafel slope values on log(i_{kin}) is shown in Fig. 10(a2), (b2), and (c2). Fig. 11 reports the polarization and power curves of the materials, and Table 4 lists the main figures of merit of MEAs' performance. It is observed that the electrochemical behaviour of PdNi-CN$_h$ 900 and PdCoAu-CN$_h$ 600 electrocatalysts is quite different from that of the Pt/C reference. The Tafel slope of the Pt/C reference starts at ca. 50–75 mV decade^{-1} and increases monotonically on current density up to about 100 mV decade^{-1}, while that of both PdNi-CN$_h$ 900 and PdCoAu-CN$_h$ 600 present initial values of 30 mV decade^{-1} or lower, which rise up to values of 100–120 mV decade^{-1} at higher current densities. In addition, with respect to PdNi-CN$_h$ 900, the Tafel slope of PdCoAu-CN$_h$ 600 is lower by ca. 20 mV decade^{-1}. A comparison between the data reported in Fig. 10(a2), (b2) and (c2) indicates that the Tafel slope of the Pt/C reference (see Fig. 10(a2)) is not significantly affected by the type of oxidant used at the cathodic side. On the other hand, the Tafel slopes of both PdNi-CN$_h$ 900 and PdCoAu-CN$_h$ 600 present values which are decreased by ca. 20 mV decade^{-1} when the oxidant is changed from air to pure

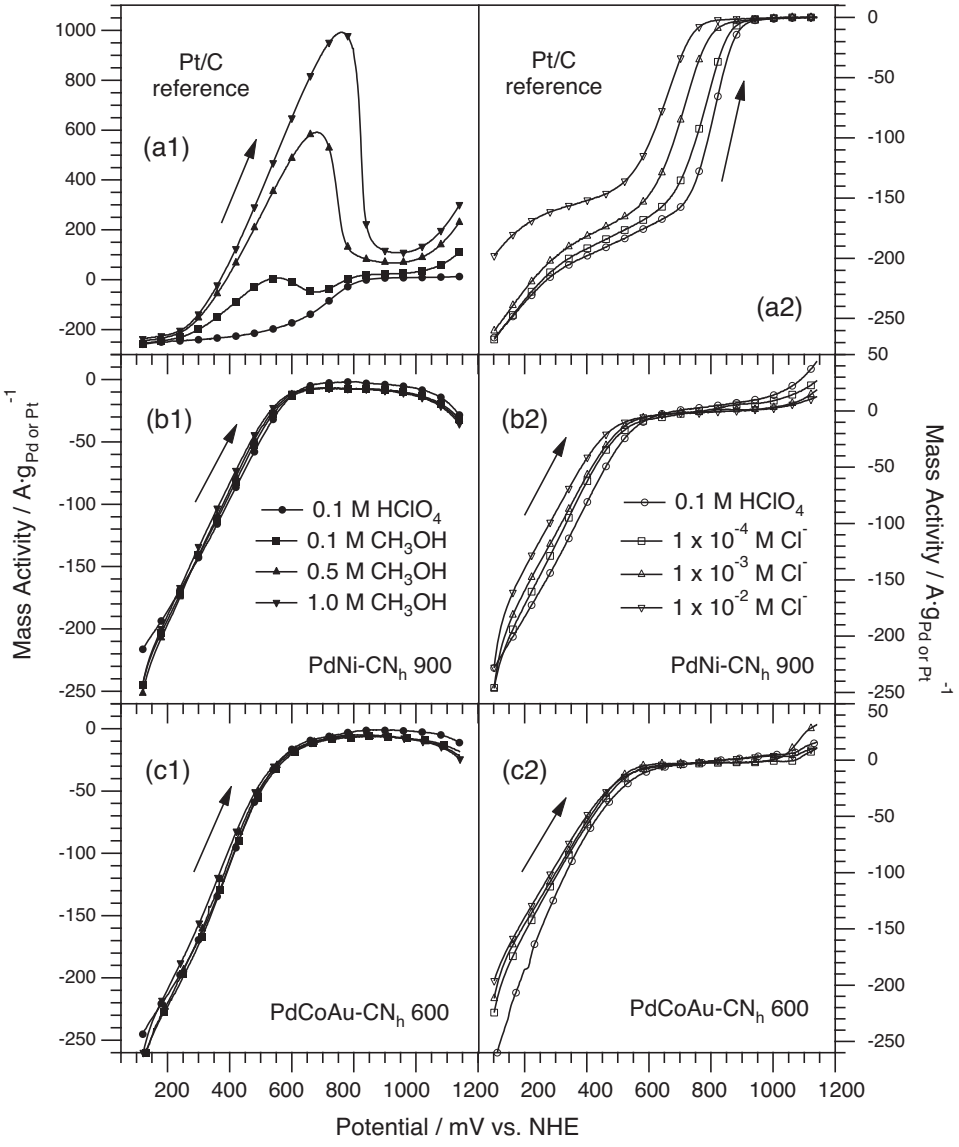

Fig. 9. Effect of increasing methanol ((a1), (b1) and (c1)) and chloride anion concentration ((a2), (b2) and (c2)) on the ORR performance of the proposed electrocatalysts.

oxygen. It is noteworthy that, with respect to the Pt/C reference, the effects of the oxygen partial pressure on the performance of both PdNi-CN_h 900 and PdCoAu-CN_h 600 are higher. Furthermore, when the oxidant is changed from air to O_2, the operating potential at 50 A $g_{Pd,\,Pt}{}^{-1}$: (a) in the Pt/C reference increases by 20 mV; (b) in both PdNi-CN_h 900 and PdCoAu-CN_h 600 increases by ca. 50 mV. The effect of the oxygen partial pressure on the performance at $V \approx 0.3$–0.5 V is also significant. In these conditions, the minimum mass of PGM to achieve 1 kW is determined. This value increases by a factor of 1.22 for the Pt/C reference and by a factor of ca. 2 for both PdNi-CN_h 900 and PdCoAu-CN_h 600 changing pure oxygen with air as the oxidant at the cathodic side. Furthermore, with respect to the Pt/C reference, the ORR overpotential at 50 A $g_{Pd,\,Pt}{}^{-1}$ of PdNi-CN_h 900 and PdCoAu-CN_h 600 results ca. 190 and 160 mV higher, respectively. However, when oxygen is adopted as the oxidant, with respect to the Pt/C reference a smaller amount of PGM is required for both PdNi-CN_h 900 and PdCoAu-CN_h 600 to achieve 1 kW of power (respectively 0.75 and 0.51 g_{Pd} vs. 1.12 g_{Pt} of the Pt/C reference). This evidence, together with the higher abundance and lower cost of Pd in comparison with Pt, makes this family of materials worthy of further research efforts despite their higher ORR overpotential.

Table 4
Performance of the MEAs prepared with the proposed electrocatalysts.

Product	Oxidant	Cell potential at 50 A $g_{Pd,\,Pt}{}^{-1}$ (V)	Difference in cell potential at 50 A $g_{Pd,\,Pt}{}^{-1}$ in air and in O_2 (mV)	Minimum PGM mass to achieve 1 kW (g)	Ratio between the minimum PGM mass to obtain 1 kW in air and in O_2
PdNi-CN_h 900	Air	0.642	50	1.45	1.93
	O_2	0.692		0.75	
PdCoAu-CN_h 600	Air	0.679	47	1.03	2.02
	O_2	0.726		0.51	
Reference MEA	Air	0.864	19	1.37	1.22
	O_2	0.883		1.12	

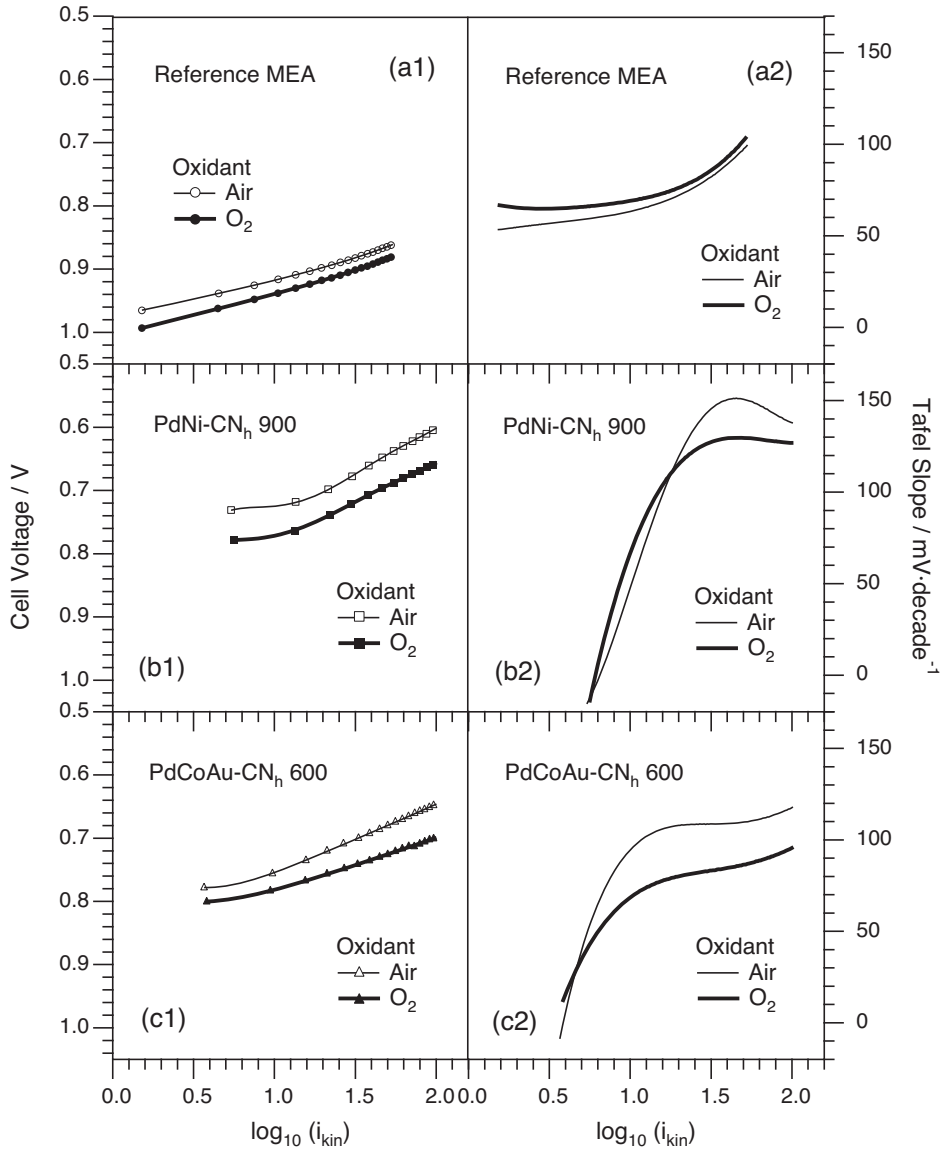

Fig. 10. Tafel plots ((a1), (b1) and (c1)) and corresponding Tafel slopes ((a2), (b2) and (c2)) determined from polarization curves collected at 0.1 mA s^{-1}. Tests are carried out with a 5 cm^2 single cell operating with pure H_2 on anode and either air or pure O_2 at cathode. H_2, air and O_2 flows are 800, 2000 and 1000 sccm, respectively; $T_{anode/cell/cathode}$ = 84/85/84 °C; RH = 100%; reagents back pressure 4 bar.

4. Discussion

"*Ex situ*" CV-TF-RDE measurements and data derived from single cell FC tests point out that the ORR overpotential of the electrocatalysts increases in the following order: Pt/C reference < PdCoAu-CN_h 600 < PdNi-CN_h 900. FC tests show that, with respect to PdCoAu-CN_h 600, PdNi-CN_h 900 is characterized by a higher Tafel slope. These evidence are coherent with a picture where the various materials are characterized by active ORR sites with a very different chemical composition. If the ORR is carried out with a four-electron mechanism, it is expected that its Tafel slope should be equal to: (a) ca. 120 mV decade^{-1} at high i_{kin}; (b) between 60 and 90 mV decade^{-1} at low i_{kin}. As reported elsewhere [31,53], one way to interpret these results is to consider that at the lowest ORR overpotentials the active sites become progressively clogged with an oxide layer, which blocks the ORR processes. XPS studies clearly point out that on the surface of the Pt/C reference there is only Pt(0), while: (a) on PdCoAu-CN_h 600 both Pd(0) and Pd(II) species are revealed; and (b) on PdNi-CN_h 900 only Pd(II) is evidenced. The presence of Pd(II) is justified if it is admitted that on the surface electrocatalytic clusters, Pd(II) is strongly coordinated by nitrogen- or oxygen-based ligands. It should be observed that, with respect to PdNi-CN_h 900, PdCoAu-CN_h 600 is endowed with a lower ORR overpotential, probably because a significant fraction of its Pd atoms is in the (0) oxidation state owing to the neighbouring Au atoms [55,56]. In addition, it is observed that for PdNi-CN_h 900, where Pd is present mostly as Pd(II), the ORR takes place even if its Tafel slope determined in single FC tests is of ca. 120 mV decade^{-1}. These data suggest that the nitrogen-based ligands of the CN matrix are complexing efficiently the catalytic metal site in PdNi-CN_h 900. It was demonstrated that in materials where the Lewis base negatively charged nitrogen-doped carbon sites are able to coordinate a metal atom such as Fe or Co a remarkable activity in the ORR was determined [30,57]. Nevertheless, even if there is still considerable work to be done in order to clarify the exact ORR mechanism in these systems, it is proposed that the role of nitrogen in the matrix is to improve the Lewis basicity of the substrate, thus stabilizing the metal coordination site and promoting the adsorption of the

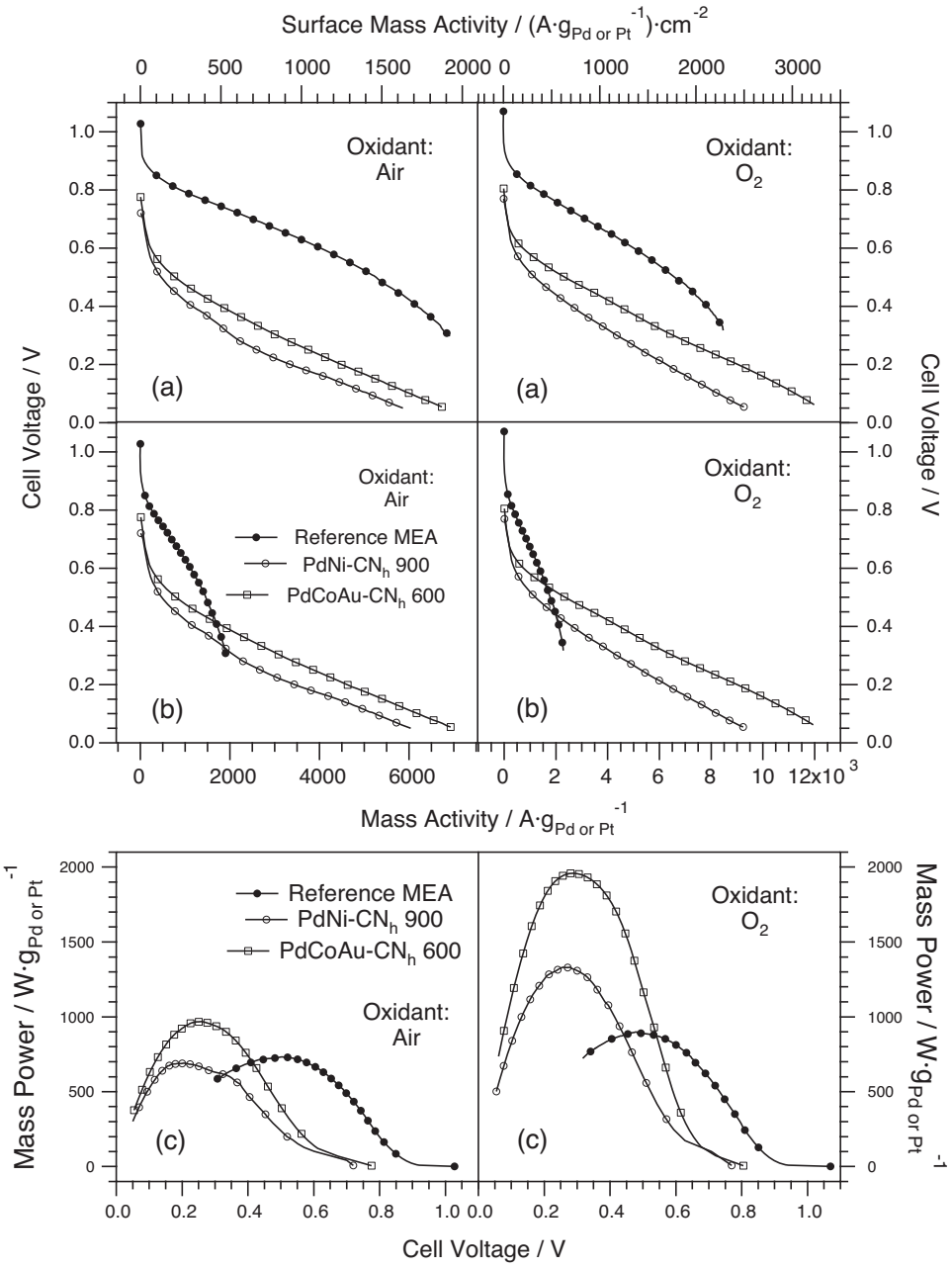

Fig. 11. Polarization curves of materials normalized on: (a) active area of the electrodes and on Pt or Pd mass; (b) Pt or Pd mass present on the cathodic electrode. (c) Electrical power profiles of prepared MEAs. Tests are carried out with a 5 cm^2 single cell operating with pure H_2 on anode and either air or pure O_2 at cathode. All the operating conditions as in the caption of Fig. 10.

O_2 molecules on the electrocatalysts [30]. It should also be pointed out that the improved stabilization of the metal coordination sites by the nitrogen atoms of the CN matrix is also assumed to be at the basis of the improved tolerance of the electrocatalysts to oxidative decomposition at high temperature, as discussed in Section 3.2. According to this hypothesis, we could suggest that one of the limiting steps in the ORR on PdNi-CN_h 900 might be the adsorption of O_2 on a Pd–N coordination complex. In these conditions, the ORR overpotential is sufficiently large that the subsequent electroreduction of oxygen and product desorption are not the rate-determining steps of the process, as suggested by the large Tafel slope. Nevertheless, the presence of Pd–O species which, as the ORR overpotential is increased, are reduced to Pd(0) cannot be excluded and may explain the capability of the PdNi-CN_h 900 electrocatalyst to oxidize hydrogen. Indeed, if all the Pd atoms are complexed by nitrogen-based ligands and thus blocked, the hydrogen oxidation reaction is not expected to take place regardless of the overpotential. PdCoAu-CN_h 600 behaves as a typical PGM-based electrocatalyst. Indeed, in this system it is expected that the ORR is carried out by Pd(0) species and Au acts as a co-catalyst, enhancing the electroreduction process. It is well-known that the oxidized Co in the active sites of the electrocatalysts behaves as a strong Lewis acid which promotes a quick desorption of the ORR products [22,23], thus improving the ORR kinetics. It is expected that a similar role is played by Ni in the PdNi-CN_h 900 electrocatalyst. It is revealed that PdCoAu-CN_h 600 oxidizes hydrogen easily. However, also in this case a contribution in the ORR from Pd–N coordination complexes cannot be excluded. The Tafel slopes of the materials as determined in single cell FC tests increase in the order: Pt/C reference < PdCoAu-CN_h 600 < PdNi-CN_h 900. With respect to air, the Tafel slopes of both

PdNi-CN_h 900 and PdCoAu-CN_h 600 decrease as they are fed with pure oxygen, while the Tafel slope of the Pt/C reference is hardly affected by the partial pressure of oxygen (PO_2). PO_2 has a strong influence on the performance of both PdNi-CN_h 900 and PdCoAu-CN_h 600, both at 50 A $g_{Pd,\,Pt}{}^{-1}$ and under "operative" potentials at 0.3–0.5 V. These evidences are attributed to the active ORR sites of the proposed electrocatalysts which are somewhat "encumbered" by the carbon nitride matrix. Indeed, with respect to the Pt/C reference, the transport of reagents and products in bulky CN materials is probably hindered and bottlenecks the operation of the electrocatalysts. On the other hand, this latter may also be one of the causes of the high tolerance of the proposed materials to the poisoning from Cl^- anions and methanol. In the Pt/C reference, the low value of the Tafel slopes determined in single FC tests at very low currents using as the oxidant both air and pure oxygen clearly evidences that the rate-determining step is the adsorption of O_2 to active metal sites. In this case, the active sites are readily available and the mass transport is not an issue. In the case of PdNi-CN_h 900 and PdCoAu-CN_h 600 materials the active sites are embedded in a CN porous matrix. Therefore, the local concentration of oxygen molecules in the neighbourhood of the active sites is probably lowered for any given PO_2 and depends on the tortuosity of O_2 diffusion channels in bulk porous nanoparticles of the electrocatalysts. As PO_2 is raised upon feeding the MEAs with pure oxygen, the surface concentration of O_2 molecules interacting with the active sites increases and the O_2 adsorption process becomes more and more significant in the modulation of the rate of the overall ORR processes, thus lowering the Tafel slope. Results suggest that the rate of the ORR processes of the proposed electrocatalysts in the low-current regime is probably depending on the "accessibility" of reagent molecules to the active sites. The "accessibility" could be hindered by two concurring effects: (a) the presence of ligands on the PGM composing the active site (as evidenced by the Pd(II) species); and (b) the reagent mass diffusion processes in bulk carbon nitride matrix through percolation pathways characterized by a high tortuosity. Indeed, results showed that the more the active sites are exposed to the reagents, the lower the Tafel plot is. Therefore, it should be highlighted that for the proposed PdNi-CN_h 900 and PdCoAu-CN_h 600 electrocatalysts the mass transfer events towards the active sites play a crucial role in modulating their performance. When the oxidant is changed from air to pure oxygen, the output power of each MEA increases significantly (see Fig. 11(c)). Correspondingly, the minimum amount of PGM to obtain 1 kW of power decreases (see Table 4). It is observed that the ratio between the PGM masses needed to yield 1 kW of power in air and in pure oxygen is similar for MEAs mounting PdNi-CN_h 900 and PdCoAu-CN_h 600 (ca. 2). The same figure determined on the reference MEA is much smaller (ca. 1.2). Taken together, in this latter case a more difficult transport of reagents is experienced by the cathodic active sites in the electrode layers formulated with the proposed electrocatalysts. These results are in accordance with the interpretation of the data collected at low currents and prompt further studies in order to optimize the morphology of the electrocatalysts, with the aim to improve their performance by reducing the tortuosity of O_2 mass transport pathways towards the ORR active sites.

5. Conclusions

In this report, an innovative synthesis protocol is described to prepare a new class of electrocatalyst for the oxygen reduction reaction (ORR) for application in PEMFC cathodes. The proposed materials, which are labeled PdNi-CN_h 900 and PdCoAu-CN_h 600, consist of graphite-like carbon nitride (CN) matrices with nitrogen content larger than 13 wt% supporting multi-metallic platinum-free clusters forming the active sites. Two different metal combinations in the multimetal clusters are investigated, Pd–Ni and Pd–Co–Au for PdNi-CN_h 900 and PdCoAu-CN_h 600, respectively. It is observed that a large concentration of nitrogen in the electrocatalysts enhances their tolerance towards oxidizing conditions and introduces a significant structural disorder in the graphitic-like structure of the support. Furthermore, in the synthesis of the proposed materials, the temperature of the pyrolysis processes T_f is a very important parameter to modulate. Indeed, T_f determines the final electrochemical properties and the structural features of the electrocatalysts. At $T_f = 600\,^{\circ}C$, the graphitization process of the CN matrix is incomplete, as witnessed by vibrational spectroscopies and XPS investigations, while at $T_f = 900\,^{\circ}C$ it is essentially complete and the nitrogen atoms are incorporated in the CN support. With respect to the PdNi-CN_h 900 electrocatalyst, PdCoAu-CN_h 600 shows an improved electrochemical performance. This result is rationalized in the framework of a general model for the ORR activity of CN-based systems based on the complexation event of metal sites by the CN ligands. Indeed, PdCoAu-CN_h 600 shows Pd(0) atoms on the surface of its active sites, which are probably stabilized by the presence of the neighbouring Au(0) species. The large concentration of nitrogen in the support acts to stabilize Pd(II) surface coordination species. In PdNi-CN_h 900 no Pd(0) species are detected and, as expected, its electrochemical activity results lower to that of PdCoAu-CN_h 600. The information derived from μ-Raman and HR-TEM investigations suggests that the active sites of both the proposed electrocatalysts are embedded in the CN matrix of the support. This observation is further supported by measurements carried out in fuel cells tested under operative conditions both in the low-current density and in the high-current density regime, and by the strong dependency of fuel cell performance on the partial pressure of oxygen. Taken together, the results permit to conclude that to improve the fuel cell performance of these very promising materials it is necessary to carry out further studies in order to learn how to modulate and improve the morphology of the support and thus address the issues highlighted here. It is to be mentioned that this paper is a fundamental study and further work is necessary to determine the long-term durability of the materials when tested in operative conditions in single-cell configuration. In conclusion, 0.75 and 0.51 g of palladium are necessary for the PdNi-CN_h 900 and PdCoAu-CN_h 600 materials, respectively, to produce the same electrical power as 1.12 g of platinum mounted in a reference fuel cell. These evidences make the electrocatalysts proposed in this work very interesting for further studies and improvements aimed at a practical application in PEMFC cathodes.

Acknowledgement

Research was funded by the Italian MURST project PRIN2008, "Direct polymer electrolyte membrane fuel cells: synthesis and study in prototype cells of hybrid inorganic–organic membranes and electrode materials".

Appendix A. Supplementary data

Supplementary data associated with this article can be found, in the online version, at doi:10.1016/j.apcatb.2011.09.034.

References

[1] W. Vielstich, in: W. Vielstich, A. Lamm, H.A. Gasteiger (Eds.), Handbook of Fuel Cells: Fundamentals, Technology, and Applications, vol. 1, John Wiley & Sons, Hoboken, NJ, 2003, pp. 26–30.
[2] R. O'Hayre, S.W. Cha, W. Colella, F.B. Printz, Fuel Cell Fundamentals, John Wiley & Sons, Hoboken, NJ, 2006, p. 8.
[3] S. Srinivasan, Fuel Cells—From Fundamentals to Applications, Springer, New York, 2006, p. 443.

[4] http://www1.eere.energy.gov/hydrogenandfuelcells/mypp/ (retrieved 11.05.11).
[5] K. Wipke, S. Sprik, J. Kurtz, J. Garbak, ECS Trans. 16 (2008) 173–184.
[6] T. Morita, K. Kojima, ECS Trans. 16 (2008) 185–198.
[7] R. Borup, J. Meyer, B. Pivovar, Y.S. Kim, R. Mukundan, N. Garland, D. Myers, M. Wilson, F. Garzon, D. Wood, P. Zelenay, K. More, K. Stroh, T. Zawodzinski, J. Boncella, J.E. McGrath, M. Inaba, K. Miyatake, M. Hori, K. Ota, Z. Ogumi, S. Miyata, A. Nishikata, Z. Siroma, Y. Uchimoto, K. Yasuda, K. Kimijima, N. Iwasita, Chem. Rev. 107 (2007) 3904–3951.
[8] J. Larminie, A. Dicks, Fuel Cell Systems Explained, 2nd ed., John Wiley & Sons, Chichester, 2003.
[9] S.S. Kocha, in: W. Vielstich, A. Lamm, H.A. Gasteiger (Eds.), Handbook of Fuel Cells: Fundamentals, Technology, and Applications, vol. 3, John Wiley & Sons, Hoboken, NJ, 2003, pp. 538–565.
[10] H.A. Gasteiger, S.S. Kocha, B. Sompalli, F.T. Wagner, Appl. Catal. B: Environ. 56 (2005) 9–35.
[11] V. Di Noto, E. Negro, J. Power Sources 195 (2010) 638–648.
[12] H.A. Gasteiger, J.E. Panels, S.G. Yan, J. Power Sources 127 (2004) 162–171.
[13] T. Tada, in: W. Vielstich, A. Lamm, H.A. Gasteiger (Eds.), Handbook of Fuel Cells: Fundamentals, Technology, and Applications, vol. 3, John Wiley & Sons, Hoboken, NJ, 2003, pp. 481–488.
[14] B. Fang, J.H. Kim, M.S. Kim, M. Kim, J.S. Yu, Phys. Chem. Chem. Phys. 11 (2009) 1380–1387.
[15] S.B. Yoon, B. Fang, M. Kim, J.H. Kim, J.S. Yu, in: G. Wilde (Ed.), Nanostructured Materials, vol. 1, Elsevier Science, Amsterdam, 2009, pp. 173–231.
[16] F.B. Su, Z.Q. Tian, C.K. Poh, Z. Wang, S.H. Lim, Z.L. Liu, J.Y. Lin, Chem. Mater. 22 (2010) 832–839.
[17] B.Z. Fang, J.H. Kim, M. Kim, J.S. Yu, Chem. Mater. 21 (2009) 789–796.
[18] D.P. Wilkinson, J. St-Pierre, in: W. Vielstich, A. Lamm, H.A. Gasteiger (Eds.), Handbook of Fuel Cells: Fundamentals, Technology, and Applications, vol. 3, John Wiley & Sons, Hoboken, NJ, 2003, pp. 611–626.
[19] T.J. Schmidt, U.A. Paulus, H.A. Gasteiger, R.J. Behm, J. Electroanal. Chem. 508 (2001) 41–47.
[20] N.M. Markovic, H.A. Gasteiger, B.N. Grgur, P.N. Ross, J. Electroanal. Chem. 467 (1999) 157–163.
[21] J.G. Oh, H. Kim, J. Power Sources 181 (2008) 74–78.
[22] V. Di Noto, E. Negro, Electrochim. Acta 55 (2010) 7564–7574.
[23] V. Di Noto, E. Negro, S. Lavina, S. Gross, G. Pace, Electrochim. Acta 53 (2007) 1604–1617.
[24] V. Di Noto, E. Negro, M. Piga, L. Piga, S. Lavina, G. Pace, ECS Trans. 11 (2007) 249–260.
[25] V. Di Noto, E. Negro, S. Lavina, N. Boaretto, M. Piga, ECS Trans. 16 (2008) 123–137.
[26] V. Di Noto, E. Negro, Electrochim. Acta 55 (2010) 1407–1418.
[27] V. Di Noto, E. Negro, R. Gliubizzi, S. Lavina, G. Pace, ECS Trans. 2 (2007) 83–91.
[28] V. Di Noto, E. Negro, R. Gliubizzi, S. Gross, C. Maccato, G. Pace, J. Electrochem. Soc. 154 (2007) B745–B756.
[29] V. Di Noto, E. Negro, R. Gliubizzi, S. Lavina, G. Pace, S. Gross, C. Maccato, Adv. Funct. Mater. 17 (2007) 3626–3638.
[30] V. Di Noto, E. Negro, G. Pace, S. Lavina, in: T. He (Ed.), Catalysts for Oxygen Electroreduction—Recent Developments and New Directions, Transworld Research Network, Kerala, 2009, pp. 195–230.
[31] V. Di Noto, E. Negro, Fuel Cells 10 (2010) 234–244.
[32] V. Di Noto, E. Negro, S. Lavina, G. Pace, PCT/IT2007/000278 patent.
[33] M. Vittadello, S. Suarez, K. Fujimoto, V. Di Noto, S.G. Greenbaum, T. Furukawa, J. Electrochem. Soc. 152 (2005) A956–A965.
[34] V. Di Noto, V. Zago, J. Electrochem. Soc. 151 (2004) A216–A223.
[35] V. Di Noto, M. Vittadello, S. Lavina, S. Biscazzo, M. Fauri, Electrochim. Acta 48 (2003) 2047–2058.
[36] V. Di Noto, M. Fauri, M. Vittadello, S. Lavina, S. Biscazzo, Macromol. Chem. Phys. 203 (2002) 354–362.
[37] V. Di Noto, M. Fauri, M. Vittadello, S. Lavina, S. Biscazzo, Electrochim. Acta 46 (2001) 1587–1594.
[38] V. Di Noto, J. Phys. Chem. B 104 (2000) 10116–10125.
[39] V. Di Noto, D. Barreca, C. Furlan, L. Armelao, Polym. Adv. Technol. 11 (2000) 108–121.
[40] V. Di Noto, J. Mater. Res. 12 (1997) 3393–3403.
[41] D.A. Shirley, Phys. Rev. B 5 (1972) 4709–4714.
[42] J.F. Moulder, W.F. Stickle, P.E. Sobol, K.D. Bomben, in: J. Chastain (Ed.), Handbook of X-ray Photoelectron Spectroscopy, Perkin-Elmer, Eden Prairie, 1992.
[43] X-ray Photoelectron Spectroscopy Database 20, Version 3.4, National Institute of Standards and Technology, Gaithersburg, MD. http://srdata.nist.gov/XPS.
[44] P. Riello, P. Canton, G. Fagherazzi, J. Appl. Crystallogr. 31 (1998) 78–82.
[45] E. Negro, V. Di Noto, J. Power Sources 178 (2008) 634–641.
[46] D. Lin-Vien, N.B. Colthup, W.G. Fateley, J.G. Grasselli, The Handbook of Infrared and Raman Characteristic Frequencies of Organic Molecules, Academic Press, Boston, MA, 1991.
[47] A. Sadezky, H. Muckenhuber, H. Grothe, R. Niessner, U. Pöschl, Carbon 43 (2005) 1731–1742.
[48] D.M. Adams, Metal–Ligand and Related Vibrations, Edward Arnold Ltd., London, 1967.
[49] F. Tuinstra, J.L. Koenig, J. Chem. Phys. 53 (1970) 1126–1130.
[50] PCPDFWIN Database, Version 2.1, 2000, #87-0640.
[51] PCPDFWIN Database, Version 2.1, 2000, #75-2078.
[52] T.J. Schmidt, H.A. Gasteiger, in: W. Vielstich, A. Lamm, H.A. Gasteiger (Eds.), Handbook of Fuel Cells: Fundamentals, Technology, and Applications, vol. 2, John Wiley & Sons, Hoboken, NJ, 2003, pp. 316–333.
[53] M. Gattrell, B. MacDougall, in: W. Vielstich, A. Lamm, H.A. Gasteiger (Eds.), Handbook of Fuel Cells: Fundamentals, Technology, and Applications, vol. 2, John Wiley & Sons, Hoboken, NJ, 2003, pp. 443–464.
[54] J.X. Wang, F.A. Uribe, T.E. Springer, J. Zhang, R.R. Adzic, Faraday Discuss. 140 (2008) 347–362.
[55] M. Chen, D. Kumar, C.-W. Yi, D.W. Goodman, Science 310 (2005) 291–293.
[56] Y.-L. Fang, J.T. Miller, N. Guo, K.N. Heck, P.J.J. Alvarez, M.S. Wong, Catal. Today 160 (2011) 96–102.
[57] M. Lefèvre, E. Proietti, F. Jaouen, J.P. Dodelet, Science 324 (2009) 71–74.